# Microwave signal emission in spin-torque vortex oscillators in metallic nanowires: Experimental measurements and micromagnetic numerical study

F. Abreu Araujo,[1,*] M. Darques,[1,†] K. A. Zvezdin,[2,3] A. V. Khvalkovskiy,[2,4,‡] N. Locatelli,[4] K. Bouzehouane,[4] V. Cros,[4] and L. Piraux[1]

[1]*Institute of Condensed Matter and Nanosciences, Université catholique de Louvain, Croix du Sud 1, BE-1348 Louvain-la-Neuve, Belgium*

[2]*A. M. Prokhorov General Physics Institute, RAS, Vavilova, 38, 119991 Moscow, Russia*

[3]*Istituto P.M. srl, Via Grassi 4, I-Torino, Italy*

[4]*Unité Mixte de Physique CNRS/Thales, 1 Ave A. Fresnel, 91767 Palaiseau, and Université Paris-Sud, F-91405 Orsay, France*

(Received 27 March 2012; revised manuscript received 3 July 2012; published 17 August 2012)

We report on microwave oscillations induced by spin-transfer torque in metallic spin valves obtained by electrodeposition of Co-Cu-Co trilayer structures in nanoporous alumina templates. Using micromagnetic calculations performed on similar spin-valve structures it was possible to identify the magnetization dynamics associated with the experimentally determined microwave emission. Furthermore it appears that in our particular geometry the microwave emission is generated by the vortex gyrotropic motion which occurs in, at least, one of the two magnetic layers of our spin-valve structures. Microwave emission was obtained in the absence of any external magnetic field with the appropriate magnetization configuration.

DOI: 10.1103/PhysRevB.86.064424 PACS number(s): 85.75.−d, 75.78.Cd, 75.47.De, 72.25.Ba

## I. INTRODUCTION

It has been shown[1–3] that the spin-torque effect predicted by Slonczewski[4] and Berger[5] can be used to overcome the Gilbert damping in such a way that it is possible to obtain coherent magnetization oscillation in magnetic spin-valve (SV) nanostructures. In these conditions the nanoscale SVs under study became the so-called spin-torque nanooscillators (STNO) that have been the subject of intensive experimental and theoretical investigations during the last decade. Initially[1–3] the STNOs used single-domain-like magnetization distribution for the free magnetic layer of the SV. Recently,[6–13] focus has been directed to another very promising and naturally stable magnetization distribution in nanoscale magnetic layers with adequate aspect ratio: the magnetic vortex state.

The vortex state constitutes one of the possible ground magnetic states of soft ferromagnetic submicrometer elements. Such a topological magnetization distribution originates from the interplay between the magneto-static and exchange energy and is characterized by an in-plane closed flux domain structure with a vortex core at the center where the magnetization turns out of plane to minimize the high energetic configuration of antialigned moments.

For suitable current and magnetic field conditions and even without[7,9,13] any magnetic field, the vortex state can be excited by the injection of a dc current through an STNO stack. The vortex dynamical excitation of interest is the gyrotropic motion of the vortex core driven by the spin-transfer-torque (STT) effect. Using both the gyrotropic vortex motion and the GMR (or TMR) electrical measurements it was possible to obtain more coherent[7,13] and larger power output[9,13,14] microwave signals than previously with uniform mode oscillations.

However, these microwave emission linewidth and output power should still be improved in order to reach the values required for the targeted telecommunication applications. A commonly believed solution to overcome this issue is to synchronize several STNOs. Although coherent emission of a small number has been observed in a few studies involving a parallel connection of STNOs,[9,15,16] the extension of such synchronization to large arrays of STNOs implies both fundamental[17] as well as important technical challenges. In addition, a series connection of STNOs[18–21] is very desirable, which is difficult to achieve using standard lithographically defined STNOs because of the relatively large aspect ratio that is required. This last issue may be tackled using a bottom-up template-based approach for the fabrication of STNOs.[22,23] By successive electrodeposition of metallic spin valves into the pores of alumina template, each of them being separated by a nonmagnetic spacer, STNO stacks connected in series can be obtained. This technique has a real potential to fabricate, in an extremely cheap, fast, and easy way, a dense array of long nanowires (NWs), each of them potentially containing about 10 STNOs in series.

In this work, we present a combined micromagnetic simulation and experimental investigation of the spin-transfer-induced vortex precession in metallic spin-valve electrodeposited nanowires. Theoretical predictions based on micromagnetic simulations are discussed in Sec. II. In Sec. III the experimentally obtained microwave emissions are compared to the theoretical predictions.

## II. MICROMAGNETIC SIMULATIONS

For the micromagnetic simulations a circular metallic SV nanopillar of 80 nm in diameter is considered. The studied SV consists in a Co(7 nm)/Cu(13 nm)/Co(24 nm) stack as shown in Fig. 1. The parameters for the magnetic properties of Co are as follows: $A = 1.3 \times 10^{-6}$ erg/cm, $\alpha = 0.011$,[24] $M_s = 1200$ emu/cm$^3$,[25] where $A$, $\alpha$, and $M_s$ are, respectively, the exchange stiffness constant, the Gilbert damping parameter, and the saturation magnetization. The smaller value of $M_s$ compared to $M_s = 1422$ emu/cm$^3$ for pure Co as well as the absence of magneto-crystalline anisotropy[23] are chosen to reproduce the experimental parameters known for electrodeposited nanowires. Indeed, as both ions of Co and Cu are present in the electrolyte solution the Co layers contain

 

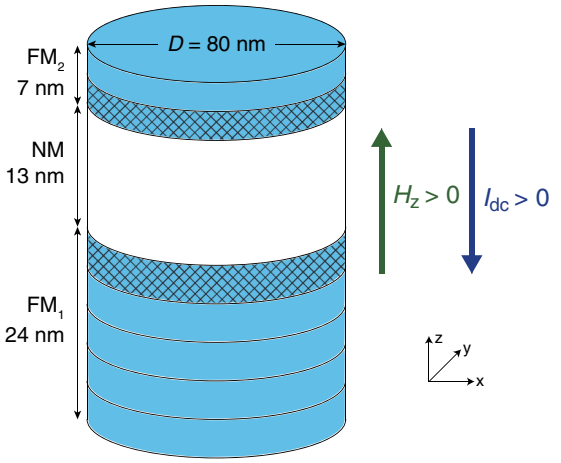


FIG. 1. (Color online) Sketch of the SV stack used in the micromagnetic simulations ($FM_1 = FM_2$ = cobalt; NM = copper). The thick magnetic layer ($FM_1$) is divided into five 4.8-nm-thick sublayers and the thin magnetic layer is divided into two 3.5-nm-thick sublayers. Spin torque acts only on the hatched sublayers. The applied external magnetic field orientation and the convention direction of positive current are also shown.

atoms of Cu thus giving rise to a reduction of the $M_s$ value and to the suppression of the magneto-crystalline anisotropy.

The step of the computational mesh is 2 nm × 2 nm in the plane and 3.5 nm (respectively, 4.8 nm) in the perpendicular direction for the thin (respectively, thick) magnetic layer. The in-plane dimensions were taken to be below the exchange length $l_{ex} = \sqrt{A/(2\pi M_s^2)} = 3.8$ nm to ensure proper behavior between two adjacent discretization cells of the spin-valve system with respect to the exchange interaction.

In a CPP-GMR spin valve, the electrons of an injected dc current acquire spin polarization (due to relaxation and spin accumulation), either by passing through a so-called polarizer layer or by being reflected from the latter. As shown hereafter and unlike most of the micromagnetic simulations made until now on such types of spin valves, the magnetization of the polarizer layer is not kept fixed. The consequence is that both magnetic layers in the SV stack can act simultaneously as a polarizer and as a free layer.

The aim of the micromagnetic calculations made for the SV depicted in Fig. 1 is to identify both magnetic ground states and magnetization dynamics of the two magnetic layers ($FM_1$ and $FM_2$) that made up the SV. The resulting informations are studied as a function of the injected current and for different magnetic field intensities applied along the rod axis of the SV.

The dynamics of the magnetization is investigated using the micromagnetic solver SPINPM.[26] In this code the magnetization is resolved by numerical integration of the Landau-Lifshitz-Gilbert (LLG) equation taking into account the spin-transfer-torque (STT) effect.[4] The LLG equation with STT is written as follows:

$$\frac{\partial \mathbf{M}}{\partial t} = -\gamma \mathbf{M} \times \mathbf{H}_{\text{eff}} + \alpha \mathbf{M} \times \frac{\partial \mathbf{M}}{\partial t} + \Gamma_{\text{STT}}, \qquad (1)$$

where $\gamma = g\mu_B/\hbar$ is the gyromagnetic ratio [$\cong 1.76 \times 10^7$ (Oe s)$^{-1}$ in cgs units, $g$ is the electron $g$ factor, $\mu_B$ is the Bohr magneton, $\hbar$ is the reduced Plank constant] and $\mathbf{H}_{\text{eff}}$ is the effective field. The latter is the sum of the magnetostatic field, the exchange field, the Oersted field, and the anisotropy field. $\Gamma_{\text{STT}}$ is the spin-transfer-torque contribution to the LLG equation. It originates from the spin-transfer effect between the polarized electrons from the injected dc current and the electrons responsible for the magnetization in a free magnetic layer. $\Gamma_{\text{STT}}$ is divided into two components (i.e., $\Gamma_{\text{STT}} = \Gamma_{\text{CPP}} + \Gamma_{\text{FLT}}$). $\Gamma_{\text{CPP}}$ refers to the Slonczewski torque and $\Gamma_{\text{FLT}}$ refers to the fieldlike torque. Knowing that in our CPP-SV the current flows perpendicularly to the layers plane, the $\Gamma_{\text{FLT}}$ term is neglected and the $\Gamma_{\text{CPP}}$ torque is given by

$$\Gamma_{\text{CPP}} = -\gamma \frac{a_J}{M_s} \mathbf{M} \times (\mathbf{M} \times \mathbf{p}), \qquad (2)$$

where $M_s$ is the saturation magnetization, $\mathbf{p}$ is the unit vector along the magnetization direction of the polarizing magnetic layer (the layer responsible for the polarized current), and $a_J$ is the spin-torque amplitude term:

$$a_J = P \frac{\hbar}{2|e|} \frac{J}{M_s d}, \qquad (3)$$

where $P$ is the current polarization, $J$ is the current density, $|e|$ is the charge of the electron, and $d$ is the free magnetic layer thickness.

As shown in Fig. 1, only the magnetic sublayers in contact with the nonmagnetic spacer (hatched sublayers) are relevant for the STT phenomenon. These sublayers act as time-varying polarizers and feel the polarized current from each other.

In the micromagnetic simulations, a bias magnetic field ($H_z$) and a dc current ($I_{dc}$) are applied simultaneously in the out-of-plane direction. The spin-torque efficiency is enclosed in the polarization parameter $P$ with a typical value of 0.3. In our convention the current is positive when the electrons flow from the thick magnetic layer ($FM_1$) to the thin magnetic layer ($FM_2$). The calculations start with magnetizations $\mathbf{m} = (1,1,0)$ in $FM_2$ and $\mathbf{m} = (-1,-1,0)$ in $FM_1$, and the magnetization then relax to its equilibrium state. The obtained configuration is identified as the most stable one associated with the $(I_{dc}, H_z)$ couple. The same calculations are made for different combinations of $H_z$ and $I_{dc}$ (for $I_{dc}$ from −7 mA to 8 mA every 0.5 mA and for $H_z$ from 0 to 5 kOe every 0.5 kOe), and the equilibrium states are summarized in the phase diagram shown in Fig. 2.

First of all, for any $(H_z, I)$ combination, a magnetic vortex state appears in the thick magnetic layer ($FM_1$), thus confirming the stability of the vortex state in that thick FM layer. In contrast, for the thin magnetic layer ($FM_2$), a vortex state, a quasiuniform state, or a C-like state, is obtained. Figure 2 splits into two distinct regions as far as the ground magnetic state is concerned. The first one refers to the one-vortex states (U/V↑ and C/V↑) and the second one to the two-vortex states (V↑/V↑, V↑/V↓, and V↓/V↑). For a negative injected current, only (quasi-)uniform (C-like and uniform) states appear in $FM_2$ regardless of the magnetic field strength. Negative currents thus give rise to one-vortex-state STNOs. On the contrary, for positive currents, one can have either one-vortex states or two-vortex states, depending on the applied magnetic field and the current intensity. Indeed, for positive currents less than 4 mA and for relatively low magnetic fields, uniform magnetic states nucleate in $FM_2$ as seen in

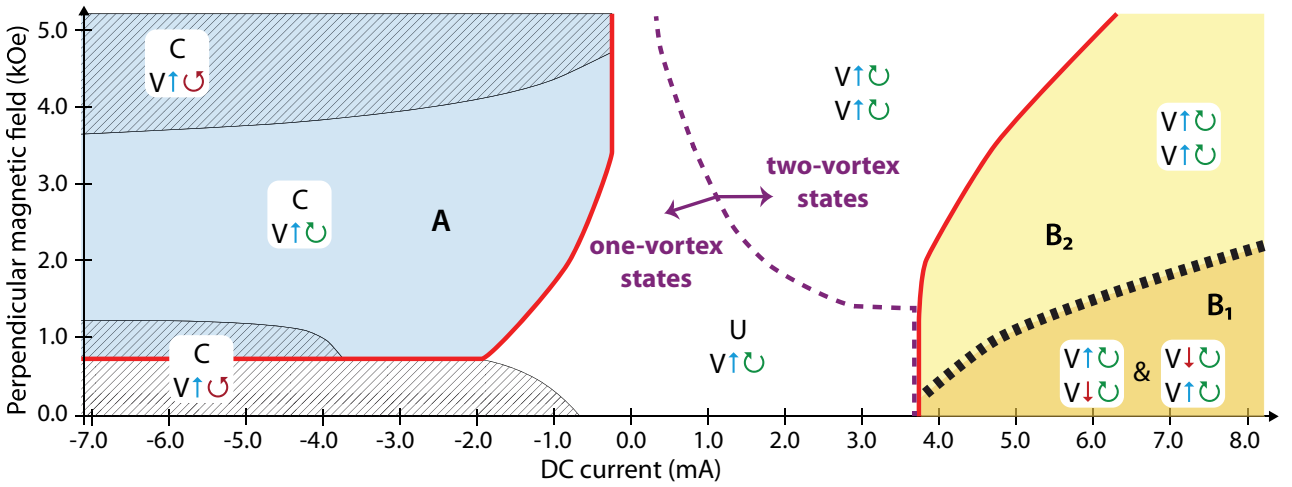


FIG. 2. (Color online) Phase diagram of the sustained vortex core oscillations driven by the spin-transfer-torque effect obtained by micromagnetic simulations. For negative currents, phase A (blue) refers to one vortex in $FM_1$ and to a C-like state in $FM_2$. For positive currents, phase B refers to two vortices, one in each magnetic layer with the same chirality and with opposite polarities (phase $B_1$, dark yellow) or with the same polarity (phase $B_2$, yellow). In the other regions, the vortex core oscillations are not maintained steadily. The notations are as follows: U, quasiuniform magnetic state; C, C-like quasiuniform magnetic state; V↑, vortex with up polarity; V↓, vortex with down polarity; ↻, clockwise chirality; and ↺, anticlockwise chirality.

Fig. 2. For larger current intensity and/or larger magnetic field amplitude one obtains two-vortex-state STNOs.

The conditions for sustained oscillations driven by the STT effect can be identified from the phase diagram shown in Fig. 2 (see colored phase A and phase B). For the other regions in the phase diagram, the vortex core oscillations are not maintained in a steady-state oscillating regime and the vortex motion is damped to the equilibrium position. In our SV system, the magnetization dynamics originates from the vortex gyrotropic motion, which occurs at least in $FM_1$. Thus we refer hereafter to this oscillator as the spin-torque vortex oscillator (STVO).

In the case of negative injected dc currents the persistent dynamical magnetic state is characterized by a vortex in $FM_1$ and a quasiuniform state (i.e., a C-like state) in $FM_2$. The steady-state oscillations are observed above a threshold bias out-of-plane magnetic field and dc current. In contrast to the one-vortex state STVO (phase A in Fig. 2), there is a persistent dynamical state for positive dc currents in which both magnetic layers exhibit vortex states (phase B in Fig. 2). Furthermore, phase B splits into two subphases, with vortices that have cores with the same and opposite polarities, that is, phase $B_2$ and phase $B_1$, respectively.

The asymmetric response for positive and negative injected currents (see Fig. 2) is due to the fact that $FM_1$ is thicker than $FM_2$ and thus constitutes a better polarizer. So for a positive (respectively, negative) current, that is, when electrons flow from $FM_1$ to $FM_2$ (respectively, from $FM_2$ to $FM_1$), the STT effect tends to align (respectively, antialign) the magnetic moments. Since a vortex state is always present in the thick $FM_1$ layer, a vortex state in $FM_2$ is favored for positive currents and the chirality imposed by the Oersted field is also stabilized by the torque effect. Reversely, for negative currents there is a competition between the Oersted field and the torque effect resulting in a C state in $FM_2$ with antialigned spins relative to $FM_1$.

The STVOs in phase $B_1$ require larger threshold currents than the C-like/V↑ states of phase A but have the remarkable property of exhibiting sustained oscillation even without any bias magnetic field $H_z$. The latter feature refers to the particular case where the vortex polarities of the two FM layers are opposite as observed in recent experiments reported by N. Locatelli *et al.*.[13]

For positive currents, the chirality of the vortices is always clockwise as it is dictated by the Oersted field induced by the current. In contrast, for negative currents the two chiralities can be observed. According to the Oersted field, negative currents favor the counterclockwise chirality (see hatched area in phase A in Fig. 2) but there is also a large area in the phase diagram where the chirality is clockwise. This particular behavior may arise from the competition between the Oersted field and the spin-torque effect that favors the antialignment of the moments between the vortex state in $FM_1$ and the C state in $FM_2$ for negative currents. However, the shape of the hatched area indicates that the competition between the different contributions to the effective field can be much more complicated.

To go further in the STVOs frequency vs magnetic field characterization, an original tool for the postprocessing of the micromagnetic simulations was developed. In this case, a dc current $I_{dc}$ is kept constant and the external applied magnetic field $H_z$ is varied in time following a linear field ramp. By continuously changing the magnetic field, the vortex core orbital oscillation also changes and a ramp speed is chosen in such a way that the vortex motion "adapts" to the applied magnetic field. In other words, the ramps are slow enough to allow the vortex motion to relax to the frequency it would have if the field was kept constant. By ramping down the magnetic field it appeared that a ramp speed of the applied field of about 50 Oe/ns is slow enough to extract reliable frequency vs magnetic field features.

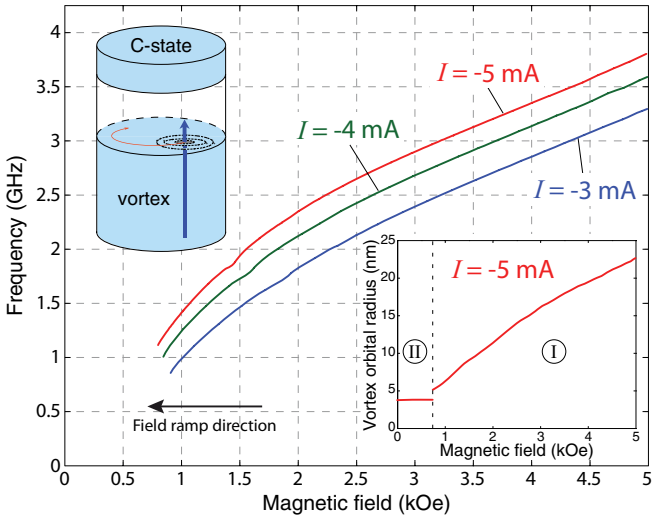


FIG. 3. (Color online) Evolution of the vortex core frequency as a function of the magnetic field (along the $z$ axis) for selected injected negative currents ($I_{dc} = -3$, $-4$, and $-5$ mA) obtained by micromagnetic simulations. The curves refer to phase A STVOs in Fig. 2. The inset shows the vortex core orbital radius vs magnetic field for $I_{dc} = -5$ mA for the oscillating regime (I), and gives also the static shift of the vortex core center in the nonoscillating regime (II).

After running the above-described simulations to characterize the frequency feature of the STVOs, a time-frequency analysis was performed. To this aim, a standard Fourier-transform-like analysis was first performed. However, since the frequency of interest is related to the vortex core gyrotropic motion, the "instant frequency" was also extracted using the position of the vortex core center. This position has been determined using a two-dimensional interpolation algorithm developed for that purpose.

### A. Negative currents—one-vortex-state STVOs

Starting from the C-state/V↑ STVO configuration of phase A a decreasing magnetic field ramp is applied from 5 kOe down to zero. The resulting frequency vs field features for the vortex gyrotropic motion in the thick magnetic layer are shown in Fig. 3 for different negative currents. The quasiuniform magnetic state (C state) in the thin magnetic layer also oscillates at the same frequency as the vortex core in the thick magnetic layer. In addition, the inset of Fig. 3 displays the vortex core orbital radius vs field for an injected dc current of $-5$ mA.

Figure 3 shows that the vortex core gyrotropic oscillation frequency decreases with a decreasing magnetic field until it reaches a threshold field under which no maintained oscillations arise. At low magnetic field (<0.9 kOe) the $z$ component of the magnetization, responsible for the STT effect, becomes too small. As a consequence, the constant $I_{dc}$ injected is no more sufficient to drive the sustained oscillations of the vortex core in the thick magnetic layer ($FM_1$).

The features in Fig. 3 exhibit two oscillating regimes. At high field (from 5 kOe down to about 2.5 kOe), the frequency is linear with respect to the magnetic field At low field, the frequency is nonlinear with respect to the magnetic field as decreasing the field destabilizes the dynamics of the C-state/V↑ configuration. Indeed, the magnetic field favors the steady-state oscillation of the vortex core because the vortex gyrotropic orbital radius decreases rapidly with the field (see inset of Fig. 3) and for small orbital radii the STT effect induced by the injected current becomes very weak.

Looking more closely at the inset of Fig. 3 one may notice almost the same field dependence for the orbital radius and for the frequency in the oscillating regime. In addition to the vortex oscillation orbital radius, the inset of Fig. 3 shows the static shift of the vortex core center for the nonoscillating regime (part II of the graph in the inset). The shift of the vortex core center (in $FM_1$) is due to the radiated stray field originating from the C state in $FM_2$. As shown in the inset of Fig. 3, the shift is about 3.8 nm for $I_{dc} = -5$ mA and it depends on the magnitude of the current.

### B. Positive currents—two-vortex-state STVOs

Phase B in Fig. 2 refers to the steady oscillating two-vortex-state configurations such as V↑/V↑, V↑/V↓, V↓/V↑, and V↓/V↓. The configuration V↓/V↓ is not shown in the phase diagram of Fig. 2 as it requires a negative applied magnetic field. Nevertheless, as will be shown in the following study, if the V↓/V↓ configuration is first stabilized, it is still stable for a weak positive magnetic field. The two-vortex state oscillates in a sustained mode driven by spin transfer once the injected positive current reaches a critical current value, depending on the $H_z$ value.

Furthermore, the different magnetic configurations of phase B can be reached by applying magnetic field for a full cycle to the two-vortex state. To illustrate this, starting from the phase $B_1$ STVO configuration V↓/V↑ for $I_{dc} = 6$ mA and at zero magnetic field, successive linear magnetic field ramps are applied as follows: from 0 to 5 kOe, then from 5 kOe to $-5$ kOe, and finally from $-5$ kOe to 5 kOe. The resulting frequency vs field feature is reported in Fig. 4(a).

In Fig. 4(a) one can see the different switch in polarity between states V↑ and V↓ for the two FM layers of the STVO (at $\pm 4.2$ kOe for $FM_2$ and at $\pm 0.7$ kOe for $FM_1$). The switch is marked by an abrupt jump in the frequency feature and this jump is larger when the switch refers to $FM_1$. Another remarkable property exhibited by Fig. 4(a) is that the thick magnetic layer drives the dynamics as the slope of the frequency vs magnetic field characteristics is dictated by the thick layer vortex polarity.

Considering the states V↓/V↑ and V↑/V↓ shown in phase $B_1$, it is possible to obtain the complete frequency vs magnetic field curves [see Fig. 4(b)]. Indeed, starting from a magnetic field of about 4 kOe (i.e., a field just below the switching field of the $FM_2$ vortex polarity) and thus considering the V↓/V↑ magnetic state, a decreasing magnetic field sweep is applied to the STVO. The field sweep is stopped as soon as the switching field of $FM_1$ vortex polarity is reached (at about $-3.8$ kOe). A similar magnetic field sweep is applied to the magnetic state V↑/V↓ starting from about $-4$ kOe up to 3.8 kOe (which corresponds to the switching field of the $FM_1$ vortex polarity).

As shown in Fig. 4(b), the two curves (the blue one with positive slope for state V↓/V↑ and the red one with negative slope for state V↑/V↓) are symmetric and cross each other at zero bias magnetic field. Furthermore, the oscillating

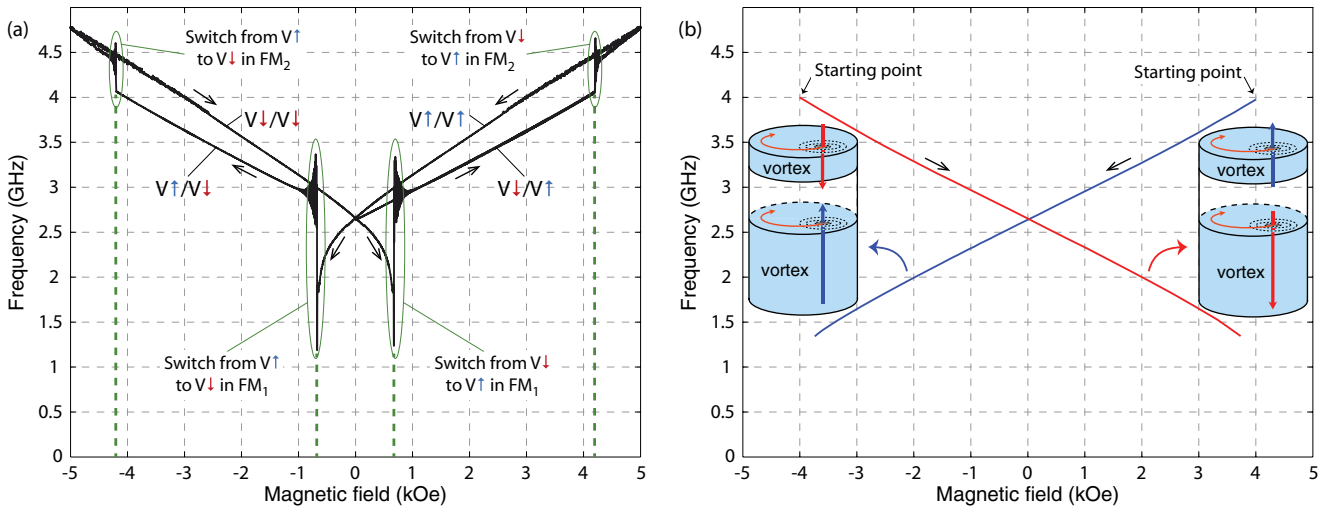


FIG. 4. (Color online) (a) Magnetic field dependence of the vortex oscillation frequency for a full sweep in field starting from 0 to ±5 kOe and a positive injected dc current of 6 mA (phases $B_1$ and $B_2$ STVOs in Fig. 2). (b) Evolution of the vortex core frequency as a function of the applied magnetic field (along the $z$ axis) for a positive injected dc current of 6 mA (phase $B_1$ STVOs in Fig. 2).

frequency vs magnetic field features obtained are linear and their slopes are directly related to the vortex polarity of the thick magnetic layer that composes the STVO.

The above-described characteristics of phase $B_1$ in Fig. 4(b) are in good agreement with recent experimental results obtained on spin-valve nanopillars.[13] As shown in Sec. III, the microwave emission at zero field and the linear dependence of the microwave emission vs field is also measured in our experimental system based on electrodeposited multilayer NWs.

## III. EXPERIMENTAL MICROWAVE EMISSION IN SPIN-VALVE NANOWIRES

The sample fabrication process begins with the anodization of about a 1-$\mu$m-thick Al layer sputtered onto the Si/Ti/Au/Nb substrate. The nanopores in the template are formed by complete anodic oxidation of the Al layer, performed in 0.3 M oxalic acid solution at 2 °C under a constant voltage of 60 V. The pore length and pore diameter are about 1.35 $\mu$m and 90 nm, respectively. The Au layer at the bottom of the pores serves as a working electrode for subsequent electrodeposition. NWs containing a stack of six pseudo-spin-valves Co(7 nm)/Cu(13 nm)/Co(24 nm) have been electrochemically synthesized in a single bath using a pulse potential deposition technique. The composition of the electrolytic solution is as follows: Co(1 M), Cu(15 mM), $H_3BO_3$ (0.5 M). Each spin valve is separated from the former by a 100-nm-thick Cu spacer layer. Then, the pores were filled electrochemically with Cu and the filled template was thinned by mechanical polishing in such a way that the electrodeposited NWs end at the template surface. More details about the fabrication process and material characterization can be found elsewhere.[22,23] Finally, electrical nanocontacts on single wires are made using a nanolithography-based contacting technique as described in a previous work.[25] Figure 5(a) illustrates the method used to create a nanocontact onto a single wire embedded in a thin alumina template. Electric transport measurements are performed to characterize the resistance and magnetic configuration of the samples. A magnetoresistance curve obtained for a positive current of 4.8 mA is shown in Fig. 5(b). The GMR effect reaches 1.3%, corresponding to $\Delta R = 520$ mΩ. The microwave emission measurements are performed with a spectrum analyzer after a 35-dBm amplification of the output oscillating GMR signal.

Selected experimental results obtained on individual spin-valve nanowires are displayed in Fig. 6. To stabilize the magnetic vortex state at least in one of the two magnetic layers of the spin-valve nanowire, a saturating perpendicular magnetic field is first applied to the sample before a decreasing ramp of magnetic field. Experimental evidence for the presence of vortex states in the Co layers has been demonstrated by Wong *et al.*[27] on the same type of electrodeposited multilayered NWs.

By applying a perpendicular magnetic field and passing a dc current through a single NW, narrow peaks are observed in the recorded emission spectra (see one of them in the inset of Fig. 6). Figures 6 and 7 display the frequency vs magnetic field features for negative and positive injected dc currents, respectively. In both cases the microwave emission appears above a threshold dc current as predicted by the micromagnetic

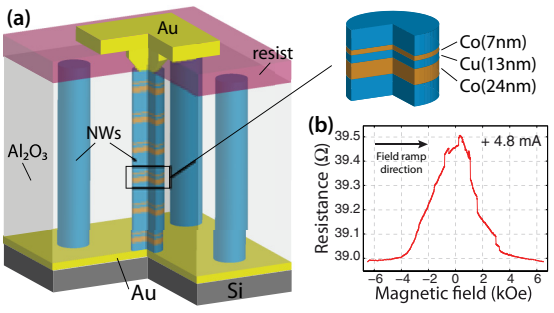


FIG. 5. (Color online) (a) Schematic drawing of template-grown NWs containing stacked STNOs and the method to connect individual NWs in an array. (b) Magnetoresistance curve measured by contacting a single NW for a positive current of 4.8 mA.

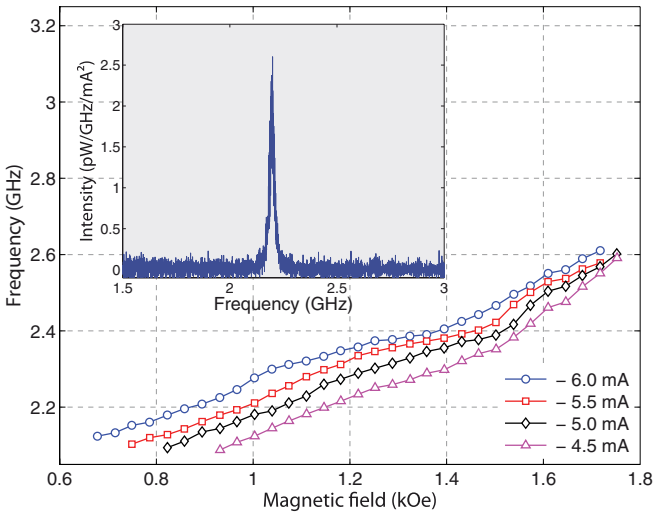


FIG. 6. (Color online) Evolution of the emitted signal frequency as a function of the perpendicular applied magnetic field. The signal was obtained by injecting negative dc currents (from −4.5 to −6 mA by steps of −0.5 mA). The inset shows the recorded spectrum for $I = -5.5$ mA and $H_z = 0.86$ kOe (linewidth = 26 MHz, power = 64 fW/mA$^2$).

simulations. Furthermore, and despite the reduced field range of emission observed, Figs. 6 and 7 display similar frequency vs magnetic field behavior as the features obtained from micromagnetic simulations for phases A and $B_1$ shown in Figs. 3 and 4(b), respectively.

Indeed, by applying a decreasing magnetic field ramp for selected negative injected dc currents, microwave signals are recorded as the magnetic field is reduced until the threshold is reached at about 0.8 kOe (see Fig. 6). These conditions correspond to the "one-vortex-state STVO" (phase A) as revealed by the above-described micromagnetic study. In addition, the positive slope of the features obtained for negative

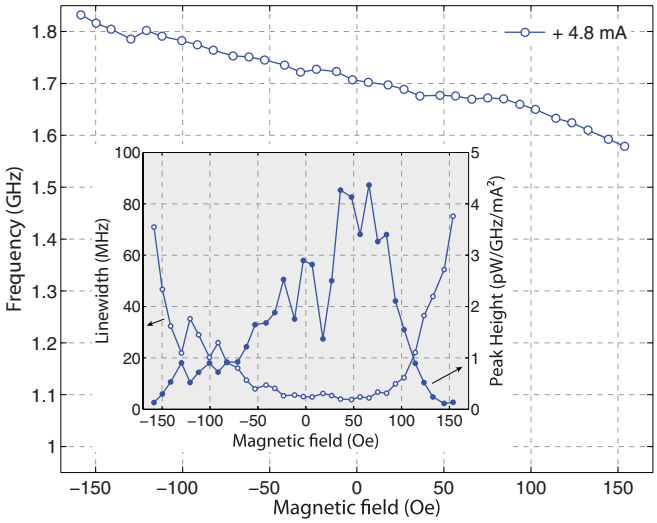


FIG. 7. (Color online) Evolution of the emitted signal frequency as a function of the perpendicular applied magnetic field. The signal was obtained by injecting a positive dc current of 4.8 mA. The inset shows the linewidth vs magnetic field and the maximum peak height vs magnetic field.

currents means that the vortex core polarity in $FM_1$ is positive (aligned with the magnetic field) as shown in the simulations but also in accordance with the experimental measurements recently reported on spin-valve nanopillars.[28]

Figure 7 displays the frequency vs magnetic field feature for a positive dc current of 4.8 mA. The experimental data are consistent with the remarkable properties of phase $B_1$ obtained by the micromagnetic simulations, that is, the microwave emission appears even without any bias magnetic field and the frequency-field characteristic is linear. As shown in the inset of Fig. 7, signal quality improvement is also obtained at zero field (i.e., the linewidth decreases with increasing peak height). The behavior reported in Fig. 7 for the measured STVO is related to the two-vortex state as shown in Fig. 4(b). According to the simulations the magnetic state responsible for the microwave emission is V↓ in $FM_1$ and V↑ in $FM_2$ [see the red curve with negative slope in Fig. 4(b)]. Nevertheless, the results reported in Fig. 7 were obtained only by sweeping magnetic field over a small range. This is likely due to the dipolar interaction between neighboring NWs in the dense array. Even if only one NW is measured electrically, the dipolar interaction between adjacent NWs destabilizes the magnetic configuration as the magnitude of the magnetic field increases.

Moreover, the relatively low linewidth observed in all the emission spectra is an argument in favor of the vortex gyrotropic motion. Indeed, the measured linewidth was as low as 3.7 MHz for a positive dc current of 4.8 mA and as low as 10.6 MHz for negative dc currents. The maximum power obtained is about 70 fW/mA$^2$ for negative currents and 35 fW/mA$^2$ for positive current. The results also corroborate the nucleation of a two-vortex state for positive currents as obtained in the micromagnetic study thus giving rise to a better spectral quality of the signal (i.e., lower linewidth and larger peak height) than for the one-vortex state obtained for negative currents. It should be mentioned that no microwave emission related to the magnetic state of phase $B_2$ appeared during the measurements. It doesn't mean that there are no steady-state oscillations corresponding to this phase, but as far as phase $B_2$ is concerned no GMR signal could be measured in our system.

Finally, it should be mentioned that no evidence for synchronization effects was observed in our measurements despite the fact that the nanowires were composed of a stacking of several Co/Cu/Co trilayers. Preliminary micromagnetic calculations indicate that the nonmagnetic metal spacer of 100 nm has to be reduced to make synchronization possible as far as the dipolar interaction is concerned.

## IV. CONCLUSION

The micromagnetic calculations performed on a pseudo-spin-valve structure, consisting of a Co(7 nm)/Cu(13 nm)/Co(24 nm) trilayer have made it possible to identify the different magnetic ground states and their dynamical behavior in our spin-valve structure. Furthermore, by sweeping the external magnetic field along the rod axis it was possible to investigate the sustained magnetization precession by considering the gyrotropic frequencies of the vortex core as a function of the applied magnetic field. Depending on the field amplitude and the injected dc current, particular magnetic configurations appear, involving

either a one-vortex state or a two-vortex state. As far as the applications are concerned, the two-vortex states (V↓/V↑ and V↑/V↓) were found to be the most promising as microwave signals, originating from the GMR effect, and can be obtained without any static bias magnetic field. In addition, the microwave signals have improved spectral quality compared to the C-state/V↑ case. The remarkable properties of the two-vortex state were corroborated by experimental results obtained on single electrically contacted nanowires fabricated by electrodeposition into nanoporous alumina templates.

As the measured microwave emission characteristics are still far from targeted applications in terms of linewidth and power, we intend to take advantage of high aspect ratio nanowires having vertically stacked Co/Cu/Co trilayers to enhance the output power by synchronizing several oscillators. Thus, the next step is to determine the appropriate spacer thickness between two STNOs to favor the synchronization by dipolar interaction.

## ACKNOWLEDGMENTS

This work was partly supported by European Union MASTER Grant No. NMP-FP7-212257, RFBR Grants No. 10-02-01162, No. 11-02-91067, and No. 12-02-01187, Federal Targeted Programs "Research and Development in Priority Areas of Russia's Scientific and Technological Complex 2007-2013," "Scientific and Scientific-Pedagogical Personnel of the Innovative Russia," CNRS PICS Russie (Grant No. 5743 2011), and the ANR agency (Grant No. VOICE PNANO-09-P231-36). Computational resources have been provided by the supercomputing facilities of the Université catholique de Louvain (CISM/UCL) and the Consortium des Equipements de Calcul Intensif en Fédération Wallonie Bruxelles (CECI) funded by the Fond de la Recherche Scientifique de Belgique (FRS-FNRS). F.A.A. acknowledges the Research Science Foundation of Belgium (FRS-FNRS) for financial support (FRIA grant).

*Author to whom correspondence should be addressed: flavio.abreuaraujo@uclouvain.be (Flavio Abreu Araujo)

†Now at LTM-CNRS/CEA-LETI, 17 rue des martyrs, 38000 Grenoble, France.

‡Now at Grandis, inc., 1123 Cadillac Court, Milpitas, CA 95035, USA.

[1] J. Katine and E. E. Fullerton, J. Magn. Magn. Mater. **320**, 1217 (2008)

[2] T. Silva and W. Rippard, J. Magn. Magn. Mater. **320**, 1260 (2008).

[3] D. Berkov and J. Miltat, J. Magn. Magn. Mater. **320**, 1238 (2008).

[4] J. Slonczewski, J. Magn. Mater. **159**, L1 (1996).

[5] L. Berger, Phys. Rev. B **54**, 9353 (1996).

[6] M. R. Pufall, W. H. Rippard, M. L. Schneider, and S. E. Russek, Phys. Rev. B **75**, 140404(R) (2007).

[7] V. S. Pribiag, I. N. Krivorotov, G. D. Fuchs, P. M. Braganca, O. Ozatay, J. C. Sankey, D. C. Ralph, and R. A. Buhrman, Nature Physics **3**, 498 (2007).

[8] Q. Mistral, M. van Kampen, G. Hrkac, J.-V. Kim, T. Devolder, P. Crozat, C. Chappert, L. Lagae, and T. Schrefl, Phys. Rev. Lett. **100**, 257201 (2008).

[9] A. Ruotolo, V. Cros, B. Georges, A. Dussaux, J. Grollier, C. Deranlot, R. Guillemet, K. Bouzehouane, S. Fusil, and A. Fert, Nature Nanotech. **4**, 528 (2009).

[10] R. Lehndorff, D. E. Buergler, C. M. Schneider, and Z. Celinski, Appl. Phys. Lett. **97**, 142503 (2010).

[11] A. Dussaux, A. V. Khvalkovskiy, J. Grollier, V. Cros, A. Fukushima, M. Konoto, H. Kubota, K. Yakushiji, S. Yuasa, K. Ando, and A. Fert, Appl. Phys. Lett. **98**, 132506 (2011).

[12] X. W. Yu, V. S. Pribiag, Y. Acremann, A. A. Tulapurkar, T. Tyliszczak, K. W. Chou, B. Brauer, Z.-P. Li, O. J. Lee, P. G. Gowtham, D. C. Ralph, R. A. Buhrman, and J. Stohr, Phys. Rev. Lett. **106**, 167202 (2011).

[13] N. Locatelli, V. V. Naletov, J. Grollier, G. de Loubens, V. Cros, C. Deranlot, C. Ulysse, G. Faini, O. Klein, and A. Fert, Appl. Phys. Lett. **98**, 062501 (2011).

[14] A. Dussaux, B. Georges, J. Grollier, V. Cros, A. V. Khvalkovskiy, A. Fukushima, M. Konoto, H. Kubota, K. Yakushiji, S. Yuasa, K. A. Zvezdin, K. Ando, and A. Fert, Nature Commun. **1**, 1006 (2010).

[15] S. Kaka, M. Pufall, W. Rippard, T. Silva, S. Russek, and J. Katine, Nature (London) **437**, 38 (2005).

[16] A. D. Belanovsky, N. Locatelli, P. N. Skirdkov, F. Abreu Araujo, J. Grollier, K. A. Zvezdin, V. Cros, and A. K. Zvezdin, Phys. Rev. B **85**, 100409 (2012).

[17] E. Iacocca and J. Akerman, J. Appl. Phys. **110**, 103910 (2011).

[18] J. Grollier, V. Cros, and A. Fert, Phys. Rev. B **73**, 060409(R) (2006).

[19] B. Georges, J. Grollier, V. Cros, and A. Fert, Appl. Phys. Lett. **92**, 232504 (2008).

[20] Y. Zhou and J. Akerman, Appl. Phys. Lett. **94**, 112503 (2009).

[21] H. Chen, J. Chang, and C. Chang, SPIN Vol. **1**, No. 1 (2011).

[22] L. Piraux, K. Renard, R. Guillemet, S. Matefi-Tempfli, M. Matefi-Tempfli, V. A. Antohe, S. Fusil, K. Bouzehouane, and V. Cros, Nano Lett. **7**, 2563 (2007).

[23] M. Darques, A.-S. Bogaert, F. Elhoussine, S. Michotte, J. de la Torre Medina, A. Encinas, and L. Piraux, J. Phys. D: Appl. Phys. **39**, 5025 (2006).

[24] M. Oogane, T. Wakitani, S. Yakata, R. Yilgin, Y. Ando, A. Sakuma, and T. Miyazaki, Jpn. J. Appl. Phys. **45**, 3889 (2006).

[25] M. Darques, A. Dussaux, A. V. Khvalkovskiy, J. De la Torre Medina, F. Abreu Araujo, R. Guillemet, K. Bouzehouane, S. Fusil, J. Grollier, G. G. Avanesyan, K. A. Zvezdin, V. Cros, and L. Piraux, J. Phys. D **44**, 105003 (2011).

[26] SPINPM is a micromagnetic code developed by the Istituto P. M. srl, Torino, Italy [www.istituto-pm.it] based on a fourth-order Runge-Kutta numerical scheme with an adaptative time-step control for the time integration.

[27] J. Wong, P. Greene, R. K. Dumas, and K. Liu, Appl. Phys. Lett. **94**, 032504 (2009).

[28] G. de Loubens, A. Riegler, B. Pigeau, F. Lochner, F. Boust, K. Y. Guslienko, H. Hurdequint, L. W. Molenkamp, G. Schmidt, A. N. Slavin, V. S. Tiberkevich, N. Vukadinovic, and O. Klein, Phys. Rev. Lett. **102**, 177602 (2009).